# Ligand Decomposition during Nanoparticle Synthesis: Influence of Ligand Structure and Precursor Selection

Breena M. Sperry, Nadzeya A. Kukhta, Yunping Huang, and Christine K. Luscombe*

ACCESS | Metrics & More | Article Recommendations | Supporting Information

**ABSTRACT:** Aliphatic amine and carboxylic acid ligands are widely used as organic solvents during the bottom-up synthesis of inorganic nanoparticles (NPs). Although the ligands' ability to alter final NP properties has been widely studied, side reactivity of these ligands is emerging as an important mechanism to consider. In this work, we study the thermal decomposition of common ligands with varying functional groups (amines and carboxylic acids) and bond saturations (from saturated to polyunsaturated). Here, we investigate how these ligand properties influence decomposition in the absence and presence of precursors used in NP synthesis. We show that during the synthesis of inorganic chalcogenide NPs ($Cu_2ZnSnS_4$, $Cu_xS$, and $SnS_x$) with metal acetylacetonate precursors and elemental sulfur, the ligand pyrolyzes, producing alkylated graphitic species. Additionally, there was less to no ligand decomposition observed during the sulfur-free synthesis of ZnO and CuO with metal acetylacetonate precursors. These results will help guide ligand selection for NP syntheses and improve reaction purity, an important factor in many applications.
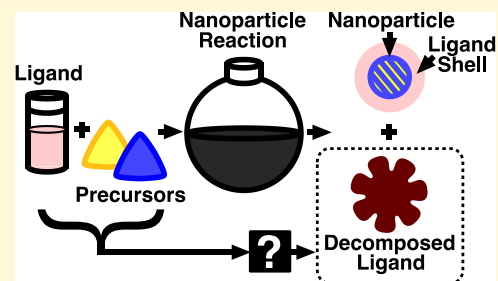
## INTRODUCTION

Nanoparticles (NPs) have drawn significant research interest among the fields of electronics, optics, magnetics, nano-biotechnology and pharmacology, catalysis, and so on.[1−8] The versatility and novelty of these NPs are owed to their unique functional properties, which are tuned by the NPs' size,[9−13] shape,[10,12,14,15] composition and defect chemistry,[10,16−18] and surface functionality.[12,19−21] One variable used to tailor these properties is ligand selection. Ligands are used in the bottom-up synthesis of NPs and can serve additional functions, including operating as a high boiling point solvent ($T_{BP} > 100$ °C), reducing agent, coordination complex, and stabilizing agent. The ligand's functions during NP synthesis have all been widely studied and reviewed.[3,20−26]

Beyond the ligands' indispensable contribution to NP synthesis, there are emerging reports that reveal that the ligand undergoes structural changes to form new products during synthesis.[27−31] These byproducts may form from structural changes in the ligand's functional group,[29−31] polymerization of the ligand backbone,[27] or ligand decomposition into graphitic materials.[28] The latter instances result in carbon impurities that exist alongside the synthesized NPs and are of interest to mitigate.[27,28] For example, the 1-octadecene ligand has been reported to autopolymerize during the synthesis of chalcogenide and metal oxide NPs, which is attributed to the heightened reactivity of the ligand's terminal double bond ($\alpha$-olefin) and potentially the metal precursor's ability to catalyze olefin polymerizations.[27] Oleylamine (OLA) and other olefins have been shown to polymerize into polysulfides in the presence of elemental sulfur,[32−34] a

common precursor used in chalcogenide NP syntheses.[32−39] In our previous work, during the synthesis of $Cu_2ZnSnS_4$ (CZTS) NPs with elemental sulfur and the OLA ligand, graphitic and amorphous carbon byproducts formed.[28]

While the polymerization and aromatization of olefins have been widely studied in the field of polymer science, ligand decomposition (*i.e.*, polymerization and graphitization) during NP synthesis is an emerging observation. Traditional polymerization of olefins is most commonly achieved through the use of Ziegler−Natta and metallocene catalysts and co-catalysts,[40−45] cationic reactions with acidic reagents,[46] anionic reactions with nucleophilic reagents,[45−47] or radical reactions.[45,46] The decomposition of olefin monomers into cyclic moieties such as polycyclic aromatic hydrocarbons and nanographite can occur *via* Diel−Alder reactions,[48−50] intermolecular cyclization,[49] and thermal cracking.[49−52] Additionally, pyrolysis (*i.e.*, thermal decomposition)[48,53,54] and solvothermal treatments[48,55] of organic monomers have been used to synthesize carbon-based NPs or carbon dots. The unsaturated (olefin) organic monomers used in these studies overlap with a wide library of ligands used in NP synthesis, including $\alpha$-olefins,[41,44] amines,[32−34,55] and carboxylic
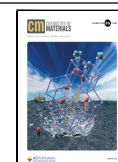
acids.[39,49−52,54,56−60] In addition to the use of ligands in these reactions, variables such as temperature and metal catalysts overlap with the temperatures and metal precursors (*e.g.*, acetylacetonates) used to synthesize NPs.[42]

Considering the aforementioned instances of ligand polymerization and graphitization both during and outside of NP synthesis, there is interest in decoupling variables (*i.e.*, ligand functional group, ligand bond saturation, and nonmetal and metal precursor selection), which results in changes to the ligands' structure. As such, this work investigates how these variables lead to unintended ligand decomposition during NP synthesis.

We began with the synthesis of kesterite $Cu_2ZnSnS_4$ (CZTS) NPs using common amine ligands with varying bond saturation (dodecylamine (DDA), oleylamine (OLA), and linoleylamine (LOA)) and analogous carboxylic acid ligands (stearic acid (SA), oleic acid (OA), and linoleic acid (LA)), as shown in Figure 1. These ligands are of interest as
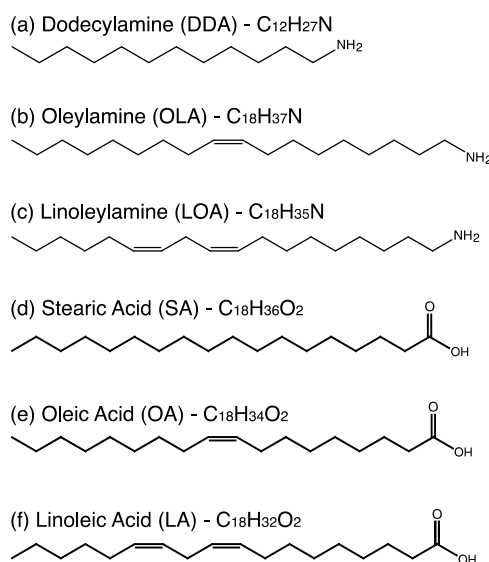


(a) Dodecylamine (DDA) - $C_{12}H_{27}N$

(b) Oleylamine (OLA) - $C_{18}H_{37}N$

(c) Linoleylamine (LOA) - $C_{18}H_{35}N$

(d) Stearic Acid (SA) - $C_{18}H_{36}O_2$

(e) Oleic Acid (OA) - $C_{18}H_{34}O_2$

(f) Linoleic Acid (LA) - $C_{18}H_{32}O_2$

**Figure 1.** Chemical structures of the ligands used in this study. This includes (a−c) amine ligands and (d, e) carboxylic ligands of varying bond saturation; unsaturated (a) DDA and (d) SA; monounsaturated (b) OLA and (e) OA; and polyunsaturated (c) LOA and (f) LA.

they are commonly used in NP synthesis and operate as a high boiling point solvent, reducing agent, and coordination complex,[3] allowing them to be the only organic monomers required for NP synthesis. CZTS was used as the model material, as in our prior work,[28] we found that pyrolyzed carbon impurities had formed in conjunction with CZTS NPs during synthesis with the OLA ligand, elemental sulfur, and with both metal acetylacetonate and metal chloride precursors. Here, we used Raman spectroscopy to identify the structure of inorganic NPs and organic products from each synthesis.

As synthesis contains external variables (*e.g.*, precursors) that may influence ligand decomposition, we systematically characterized the structural changes and stability of the ligand in the absence and presence of precursors (*i.e.*, elemental S, Cu acetylacetonate, Zn acetylacetonate, and Sn acetylacetonate). This enabled us to directly study the influence of ligand bond saturation, functional group, and precursor selection on ligand decomposition. Through structural (Raman spectroscopy) and thermal (thermal gravimetric analysis, TGA) analyses, we found that bond saturation, functional group, and sulfur

content influence the pyrolysis, or thermal decomposition, of the organic ligand; ligands which contain double bonds have amino groups and ligands which are heated in the presence of elemental sulfur are inclined to form graphitic species. Additionally, we find that the individual elements selected ($M$ = Cu, Zn, Sn) for NP synthesis also contribute to *in situ* ligand decomposition to different extents.

## 2. METHODS

**2.1. Materials.** Ligands used in this study include dodecylamine (98%, Aldrich), octadecylamine (98%, Aldrich), oleylamine (70%, Aldrich), stearic acid (98%, Aldrich), oleic acid (99%, Aldrich), and linoleic acid (99%, Aldrich). Linoleylamine is not commercially available and therefore was synthesized (see the SI for our synthetic protocol and material confirmation). Metal precursors used in NP synthesis include copper(II) acetylacetonate (99.99%, Aldrich), zinc(II) acetylacetonate (99.995%, Aldrich), and tin(IV) bis-(acetylacetonate) dibromide (98%, Aldrich). Elemental sulfur (99.98%, Aldrich) is used in the ligand−sulfur mixture and operates as the chalcogen precursor during NP synthesis. Solvents include isopropanol and toluene. Substrates include glass slides and soda lime glass sputtered with Mo (Mo/SLG).

Due to the relatively low purity of oleylamine (70%), the ligand was purified, following the procedure by Baranov et al.[61] This was to eliminate common impurities in OLA, such as oxygen containing unsaturated amides and nitroalkanes.[61] For comparison, all experiments and results were repeated with the purified oleylamine (70%) (see Figure S2). Additionally, in this work, short-chain dodecylamine ($C_{12}H_{27}N$) was used as the saturated amine rather than octadecylamine (ODA; $C_{18}H_{39}N$) since the synthesis of CZTS was unsuccessful with the ODA ligand (see Figure S3) and DDA had been previously used to synthesize CZTS NPs.[62]

**2.2. 1 M Ligand−Sulfur Mixtures.** A concentration of 1 mmol of elemental sulfur (32 mg) in 1 mL of ligand was used to form all 1 M ligand−sulfur mixtures. Oleylamine and linoleylamine were heated to 40 °C to form a homogeneous solution with sulfur, whereas dodecylamine (solid at room temperature, $T_{MP}$ = 28 °C) was heated to 80 °C. Upon heating and mixing amine−sulfur, all solutions turned red−orange in color and remained homogeneous upon cooling to room temperature. Unlike amine−S mixtures, homogeneous carboxylic acid−S solutions did not form at temperatures below the melting point of elemental sulfur (112 °C), and upon cooling, elemental sulfur precipitated from the carboxylic acid−sulfur mixture. As such, these solutions were mixed and held at 115 °C to form a homogeneous clear solution until used for further experimentation or characterization.

**2.3. NP Synthesis.** The metal precursors, the selected ligand, and a stir bar (for continuous stirring) were sealed in a 100 mL three-neck round bottom flask, which was transferred to a Schlenk line for air-free chemistry. To degas the mixture of trapped gases and volatiles, the flask was cycled a minimum of 3 times between vacuum and $N_2$ over 0.5 h at room temperature. Using a heating mantle, the flask was then heated to 130 °C and further degassed for 1 h until bubbling commenced under vacuum. Under $N_2$ flow, the solution was heated to 225 °C at a rate of ∼10 °C/min. For chalcogenide NP syntheses, upon reaching 225 °C, the flask was injected with the separately prepared 1 M ligand−sulfur solution. After stirring at 225 °C for 2 h, the flask was raised from the heating mantle and naturally cooled down to 80 °C. A solution of 5:1 antisolvent to solvent was poured into the flask. The solution was centrifuged (13.5 K rpm, 10 min), followed by decanting. Sedimented NPs were dispersed in a 3:1 solution of antisolvent to solvent, where the centrifuging (12k rpm, 5 min) and decanting processes were repeated. Residual solvent was removed with a rotavapor and samples were further dried for 24 h under vacuum prior to characterization, forming a powdered NP sample. For further details on the molar ratios of precursors, ligand concentrations, and washing procedures used during the synthesis of CZTS, metal (Cu, Zn, Sn), and chalcogenide NPs (Cu−S, Zn−S, Sn−S), see the SI.
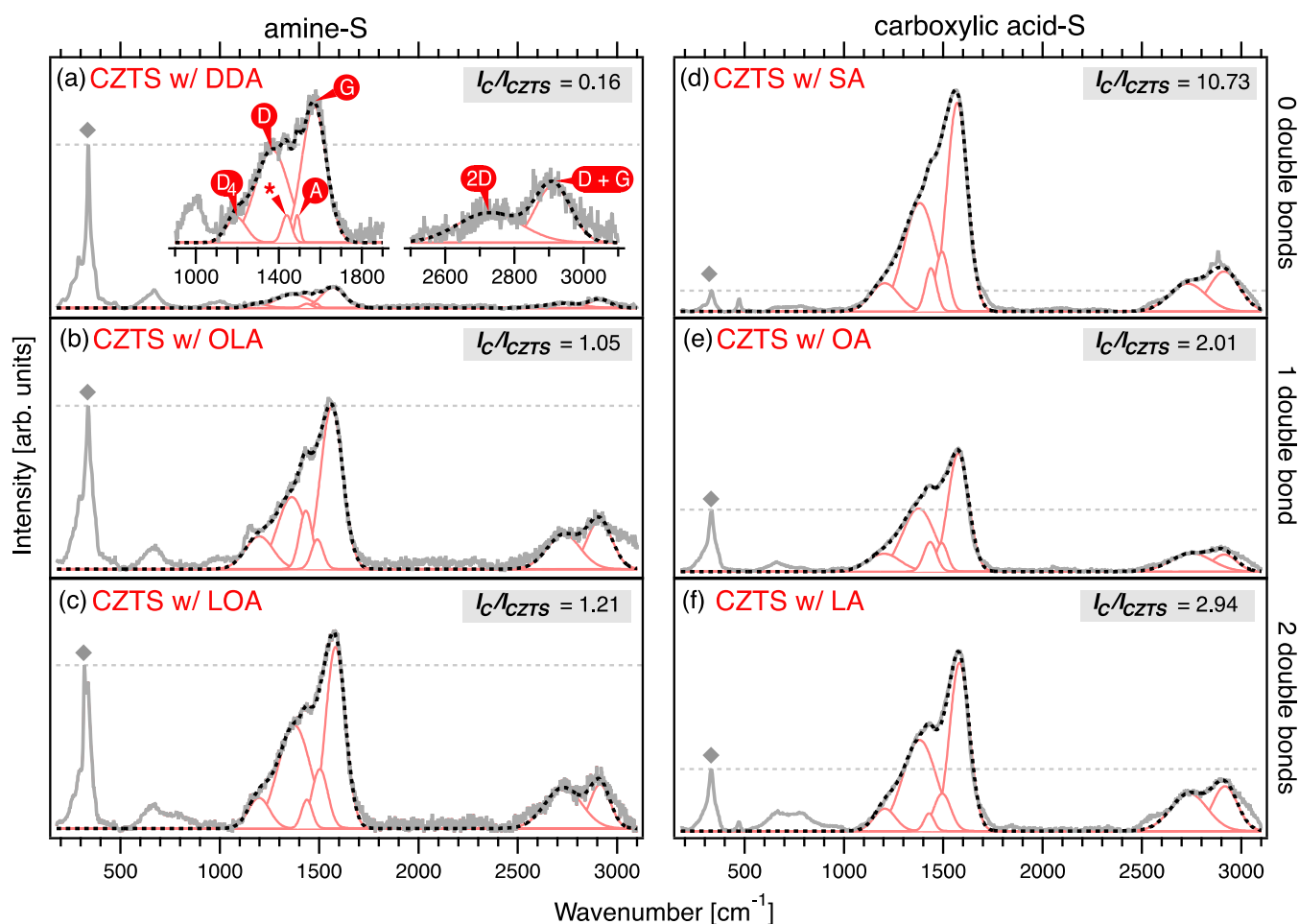
**Figure 2.** Raman spectra for all CZTS NPs synthesized with ligands of varying functional groups and bond saturation. CZTS samples were synthesized with either (a, b, d) amines and (d, e, f) carboxylic acid ligands, and the ligand had either (a, d) no double bonds, (b, e) one double bond, or (c, f) two double bonds. The relative intensities of amine spectra are comparable, and the intensities in panels (e) and (f) are comparable. Deconvoluted Gaussian fits and their peak assignments are included in the spectrum (a). Across each spectrum, the signature CZTS peak at 339 cm$^{-1}$ is identified (diamond symbol), the intensity of CZTS ($I_{CZTS}$) is emphasized (dashed line), and the intensity ratio between CZTS (at 339 cm$^{-1}$) and carbon (maximum between 1000 to 1800 cm$^{-1}$, $I_C$) is listed.

## 2.4. Structural Characterization of NP Synthesis Products.

Structural characterization of synthesized inorganic NPs was carried out with X-ray diffraction (XRD), as XRD is ideal for identifying the phases of crystalline materials. XRD was collected with a Bruker D8 Discover Microfocus X-ray diffractometer under Cu K-$\alpha$ ($\lambda$ = 1.54 Å) radiation. Powdered NP samples were pressed onto a Mo/SLG substrate. All diffractograms were calibrated using the Mo substrate's (110) peak center at 40.501° (COD 9008543) and were compared against reference patterns to identify the NP structure. Crystallite size of formed NPs was estimated with the Debye–Scherrer equation applied to fitting of Lorentzian peaks. All collected XRD diffractograms, reference diffractograms, and analyses are included in Figure S8.

To further identify the NPs and to detect carbonaceous NP reaction products, a Renishaw InVia Raman confocal microscope was used on all powdered NP samples, pressed onto a Mo/SLG substrate. Raman collection and analysis were performed with a 514 nm laser (excitation wavelength), 1200 L/mm laser grating, 10 s acquisition time, and 50× microscope objective, and spectra were fitted *via* Gaussian deconvolution. Laser power, acquisition time, and accumulations were optimized for each material to circumvent laser ablation/florescence/detector saturation while maintaining adequate spectral signal to noise. Sample-specific methods, Raman spectra, and analyses accompany the XRD diffractograms in Figure S8.

## 2.5. Thermal Decomposition of Ligands and Ligand–Sulfur Mixtures.

Information on the ligand's and ligand–sulfur mixture's thermal stabilities are obtained by thermogravimetric analysis (TGA) and the first derivative of TGA (DTG), as outlined by ISO 11358-1, ASTM E2550-21, and ASTM E1131-20 standards.[63−65] Dynamic TGA was performed using a TA Instruments Q20 thermogravimetric analyzer, which measures a material's mass loss (displayed as weight percent [%]) as a function of temperature. TGA was collected *via* heating 38.6 ± 1.4 mg of material (in a platinum crucible) at a fixed rate (10 °C/min) in an inert environment (40 mL/min N$_2$).[63−65] N$_2$ was used to avoid material combustion, and the exhaust was bubbled through a NaOH solution to quench produced H$_2$S ($g$) from ligand–S mixtures. The DTG spectra were obtained from the first derivative with respect to the temperature of the TGA spectra and offered additional information on fluctuations in the rate and temperature ranges of mass loss.[63−65]

As TGA does not offer information on a material's structure, additional structural characterizations of thermally decomposed products were needed. However, residue from TGA was too minimal to collect for further characterization. To obtain larger quantities of decomposed material at elevated temperatures, 3 mL of the ligand or 3 mL of the 1 M ligand–sulfur mixture was heated in a round bottom flask with a heating mantel, following the same conditions used in NP synthesis (*e.g.*, degassing, heating rate, N$_2$). Aliquots were collected at 130 °C after 1 h, 225 °C after 2 h, and 300 °C after 2 h. To collect the sample at 500 °C, which exceeds the temperature limits of the heating mantel, 3 mL of the material was deposited into a glass scintillation vial, which was placed within a graphitic crucible. The crucible was

loaded into a tube furnace and degassed several times, alternating between vacuum and $N_2$ (5 min per cycle). Under $N_2$ flow (100 mL/min) and at atmospheric pressure, the sample was heated to 500 °C at a ramp rate of 10 °C/min to remain consistent with the conditions used during synthesis and TGA collection. Exhaust was bubbled through a NaOH solution to quench produced $H_2S$ (g). The samples were held at 500 °C for 30 min, followed by rapid cooling. Samples were exposed to air once at room temperature and collected for subsequent characterization.

**2.6. Structural Characterization of Ligands and Ligand–Sulfur Mixtures.** Structural differences in the organic ligands, ligand–sulfur solutions, and their decomposed products were characterized by both Raman spectroscopy and Fourier transform infrared (FTIR) spectroscopy, complementary vibrational spectroscopy techniques that are used to identify a materials' molecular structure.[66]

Raman spectroscopy spectra were collected with the same Renishaw InVia Raman confocal microscope used to characterize NP samples (514 nm excitation wavelength, 1200 L/mm laser grating, 10 s acquisition time, 10% laser power (0.8 mW), 50× objective magnification). Each sample was measured 10 times at different spots to ensure homogeneity. A 5th order polynomial ($R^2$ = 0.9999) background subtraction was performed on materials with high fluorescence sigmoidal backgrounds; otherwise, a fitted spline background subtraction was performed. Peak centers, breadths, and intensities were determined *via* deconvoluted Gaussian fits.

FTIR was performed using a Thermo Scientific Nicolet 8700. Prior to use, compressed $N_2$ was used to exhaust air in the system, and the detector was cooled with liquid $N_2$. Samples were deposited onto an attenuated total reflection (ATR) attachment, and data was collected under continuous $N_2$ flow (30 psi). Each FTIR spectrum is a summation of 128 acquisitions.

$^1$H NMR was additionally used to further identify changes in the ligand's structure. The Bruker AV300 spectrometer was used to collect $^1$H NMR spectra at 300 MHz. $CDCl_3$ was used as the solvent. Chemical shift offset was calibrated using the $CDCl_3$ peak centered at 7.26 ppm.

## 3. RESULTS AND DISCUSSION

**3.1. Decomposition of Amine and Carboxylic Acid Ligands during the Synthesis of CZTS Nanoparticles.** Ligand decomposition was first observed during the synthesis of kesterite $Cu_2ZnSnS_4$ (CZTS) with the commonly used monounsaturated oleylamine (OLA) ligand.[28] To screen ligands for decomposition during NP synthesis, we first synthesized $Cu_2ZnSnS_4$ (CZTS) NPs with the saturated and unsaturated amine and carboxylic acid ligands, as shown in Figure 1: DDA (saturated amine), OLA (monounsaturated amine), LOA (polyunsaturated amine), SA (saturated carboxylic acid), OA (monounsaturated carboxylic acid), and LA (polyunsaturated carboxylic acid).

Raman spectroscopy (see Figure 2) was used for the structural identification materials present after NP synthesis. The energy associated with bond vibrations and the polarizability of bonds are, respectively, captured by the Raman shifts and relative intensities within Raman spectra, enabling the precise identification of bonds within a crystal or molecule.[66,67] Across all of our synthesized NP samples, Raman spectra point to the formation of kesterite CZTS (identified by signature peaks at 289, 339, and 660 cm$^{-1}$) in addition to a carbonaceous material (1000–1800 cm$^{-1}$).

By deconvoluting our Raman signals between 1000–1800 cm$^{-1}$, we identified the presence of both graphitic and amorphous carbon (see Table 1 for all peak assignments). Graphitic carbon was identified by the highest intensity band, denoted the G- ("graphene") band.[68–75] It is apparent that this

**Table 1. Raman Assignments of Carbon Products**

| observed Raman shift [cm$^{-1}$] | assigned vibrational mode[72,74] |
|---|---|
| 1197–1205 | D$_4$-band, amorphous carbon with graphitic domains, *trans*-polyacetylene (TPA), ionic impurities |
| 1362–1381 | D-band, disordered graphitic lattice |
| 1427–1439 | unassigned |
| 1489–1502 | A-band, amorphous carbon |
| 1562–1582 | G-band, ordered graphitic lattice |
| 2729–2749 | 2D-band, second-order resonance |
| 2913–2916 | D + G-band, resonance |

graphitic carbon has high disorder, as the G-band has a broad full-width half-max and is accompanied by a lower intensity D- ("defect") band.[72] In addition to observing the G- and D-bands, we also identified the lower intensity D$_4$- and A-bands, indicating the presence of disordered graphite, polyenes, ionic impurities, or structured amorphous carbon.[72,74] Within this region, an additional peak was present across all samples between 1429 and 1439 cm$^{-1}$, which we were unable to confidently assign to known carbon or CZTS scattering bands. Further, the two low-intensity broad bands observed between 2500 and 3100 cm$^{-1}$ correspond with the second-order out-of-plane vibrations of graphene and graphite: the 2D-band[72,74] and the G + D-band.[74]

The position of the 2D-band and its relative intensity in relation to the G-band ($I_{2D}/I_G$) further identify the material's structure. For monolayer graphene, $I_{2D}/I_G$ is ~3 and its 2D-band is centered between 2680–2700 cm$^{-1}$. As disorder increases, $I_{2D}/I_G$ is reduced to ~0.3 and the 2D-band shifts to 2720–2740 cm$^{-1}$.[72] Here, we observed an $I_{2D}/I_G$ ratio of 0.20 ± 0.05 with a peak center at 2739 ± 10 cm$^{-1}$ across all samples, further confirmation of highly disordered graphitic carbon formation during the synthesis of CZTS NPs.

The breadth of the G- and D-bands, detection of D$_4$- and A-bands, and low $I_{2D}/I_G$ ratio are all consistent with the presence of alkylated graphitic flakes, highly oriented pyrolytic graphite (HOPG), graphene quantum dots, carbon dots, or soot.[48,72,74,76] As such, Raman spectroscopy reveals that all organic ligands used in this study—regardless of bond saturation or functional group—formed a highly defective graphitic carbon during CZTS NP synthesis, herein referred to as the "carbon impurity".

In addition to utilizing Raman scattering intensity for structural identification, it also offers information on material concentration, which is proportional to intensity.[66,67,77] Fluctuations in the relative intensity between CZTS NPs and the carbon impurity ($I_C/I_{CZTS}$, reported in Figure 2) directly correlate with fluctuations relative to the carbon impurity concentration across different samples.[66,67,77] From $I_C/I_{CZTS}$, it is determined that the relative concentration of carbon residue varies depending on ligand selection.

For amine-synthesized samples, as the number of bonds increased along the ligand backbone, the relative intensity of the carbon impurity increased from $I_C/I_{CZTS}$ = 0.16 (DDA, 0 double bonds) to 1.05 (OLA, 1 double bond) and to 1.21 (LOA, 2 double bonds). Notably, the observed increase in concentration was significantly more pronounced between 0 and 1 double bond (a 6.5× increase) than between 1 and 2 double bonds (1.2× increase). The *in situ* decomposition of unsaturated amines during CZTS synthesis may be attributed to the increased reactivity of olefins. This would be in agreement with a previous study in which the use of saturated
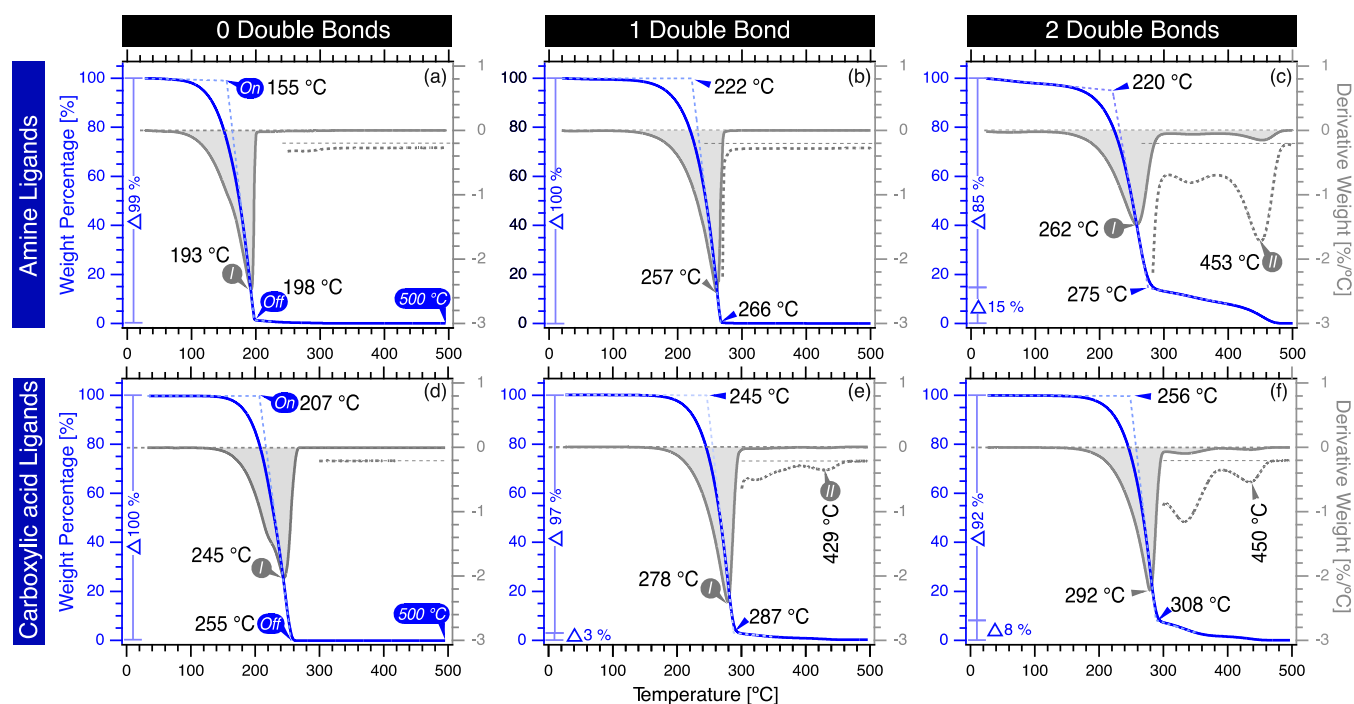
**Figure 3.** TGA (blue) mass loss profiles and overlayed derived DTG (gray) curves for (a–c) amine and (d–f) carboxylic acid ligands with varying bond saturation (0–2 double bonds). This includes (a) DDA, (b) OLA, (c) LOA, (d) SA, (e) OA, and (f) LA. For clarity, the DTG signal is amplified by 10× between 250 and 500 °C (gray dashed inset). Points On and Off along the TGA spectra correspond with the extrapolated onset and offset temperatures of thermal events, points I and II (when present) along the DTG spectra correspond with the inflection points of separate thermal events. To the left of each curve, the changes in mass loss between On and Off (wt %$_{Off}$ −wt %$_{On}$) and between the Off and 500 °C (wt %$_{500 °C}$ −wt %$_{Off}$) are labeled. From these extrapolated and extracted values, we identified relevant temperatures ($T_{On}$, $T_I$, $T_{Off}$, $T_{II}$), mass losses (wt %$_{On}$, wt %$_{Off}$, wt %$_{500 °C}$), and rates of mass loss (wt %$_I/T_I$, wt %$_{II}/T_{II}$), as listed in Table 2.

amines mitigated *in situ* polymerization ligand during NP synthesis.[27]

The concentration of carbon impurities was consistently higher for carboxylic acids than for amines. Unlike amines, carboxylic acid-synthesized samples did not exhibit the same bond saturation-dependent trend. While the concentration of carbon impurities increased similarly between 1 and 2 double bonds—a 1.5× increase between OA ($I_C/I_{CZTS} = 2.01$) and LA ($I_C/I_{CZTS} = 2.94$)—the ratio for the fully saturated carboxylic acid was considerably elevated (SA, $I_C/I_{CZTS} = 10.73$). This is contrary to what we observed with the saturated amine (DDA), which had the lowest concentration of carbon impurities across all samples.

The stark difference in SA's decomposition may be an artifact of poor NP washing after synthesis. Unlike other ligands used in this study, SA's higher melting point ($T_{MP} = 69$ °C) resulted in ligand solidification during NP washing, limiting the removal of excess ligands, reflected by the ligand backbone being detected after synthesis (CH$_2$ and CH$_3$ at 2849 and 2882 cm$^{-1}$, respectively).[66] As washing reduces excess ligands, reagents, and impurities, it is plausible that the efficacy of washing would also influence the final concentration of carbon impurities within CZTS samples synthesized with SA. Therefore, it is important to directly compare the decomposition of ligands under controlled conditions, as in the absence of precursors or other variables, including NP washing.

**3.2. Thermal Stabilities of Amine and Carboxylic Acid Ligands.** Heretofore, all ligand decomposition studies were conducted in the presence of metal and nonmetal precursors to synthesize CZTS NPs. This served to better understand the

ligands' tendency, or lack thereof, to decompose during NP synthesis. However, due to variables present during synthesis (*e.g.*, precursors, washing procedure), it is challenging to discern the contribution of the ligand's innate structure (*i.e.*, bond saturation and functional group) to the observed decomposition. To elucidate how the ligand's structure influences decomposition, we performed thermal gravimetric analysis (TGA) to investigate the ligand's intrinsic thermal stability when isolated from external variables used in NP synthesis.

A material is considered thermally stable until a thermal event begins, which is signified by the onset of mass loss (denoted as "On"). These thermal events may occur due to material vaporization, pyrolysis into volatile species, or a chemical reaction, which produces volatile species.[63,64,78] After the offset of mass loss (denoted as "Off") either no material remains or residual material is present. Generally, thermally stable residue can form from impurities included within the material from the product(s) of pyrolysis or from the product(s) of a chemical reaction. A rise in thermal stability arises from an increase in crystallinity, molecular weight, or bond energy.[79,80] These products are prevalent until exceeding the temperature threshold required for a subsequent thermal event.[63,64,78] As thermal events are bound by fluctuations in the rate of mass loss, the first derivative of TGA—known as the derivative thermogravimetry (DTG) spectra—is also used to further extract information on the apex of mass loss (denoted by "I" for inflection point) and the rates of mass loss ($\Delta$wt %/$\Delta T$).[63,64,78]

The TGA and DTG curves in Figure 3 show that under inert conditions and in the absence of all NP precursors, bond

**Table 2. Key Values Extracted from TGA and DTG of Ligand and Ligand−S Mixtures**

| | DDA | DDA-S | OLA | OLA-S | LOA | LOA-S | SA | SA-S | OA | OA-S | LA | LA-S |
|---|---|---|---|---|---|---|---|---|---|---|---|---|
| wt/wt % of S/ligand [%] | | 4.0 | | 3.9 | | | | 3.8 | | 3.6 | | 3.6 |
| boiling point $T_{BP}$ [°C] | 247 | | 364 | | | | 361 | | 360 | | 230 | |
| extrapolated onset (On) | | | | | | | | | | | | |
| $T_{On}$ [°C] wt | 155 | 144 | 222 | 193 | 220 | 202 | 207 | 208 | 245 | 243 | 246 | 236 |
| wt %$_{On}$ [%] | 99.1 | 98.2 | 98.8 | 99.7 | 95.1 | 96.5 | 99.9 | 100.0 | 99.6 | 99.9 | 99.7 | 99.9 |
| inflection point (I) | | | | | | | | | | | | |
| $T_I$ [°C] | 193 | 191 | 257 | 243 | 262 | 247 | 245 | 247 | 278 | 281 1 | 278 | 283 |
| $\Delta$wt %$_I/\Delta T_I$ [%/°C] | −2.47 | −1.52 | −2.25 | −1.14 | −1.46 | −0.97 | −2.02 | −1.96 | −2.41 | −1.8 | −2.22 | −1.24 |
| extrapolated offset (off) | | | | | | | | | | | | |
| $T_{Off}$ [°C] | 198 | 203 | 266 | 265 | 275 | 271 | 255 | 258 | 287 | 295 | 287 | 308 |
| wt %$_{Off}$ [%] | 1.4 | 12.3 | 0.4 | 17.6 | 14.5 | 32.8 | 0.1 | 0.3 | 2.9 | 10.0 | 8.3 | 17.0 |
| inflection point (II) | | | | | | | | | | | | |
| $T_{II}$ [°C] | | 347 | | 435 | 453 | 445 | | | 429 | 429 | 434 | 432 |
| $\Delta$wt %$_{II}/\Delta T_{II}$ [%/°C] | | −0.07 | | −0.13 | −0.15 | −0.31 | | | −0.01 | −0.01 | −0.03 | −0.11 |
| end of run (500 °C) | | | | | | | | | | | | |
| wt %$_{500\ °C}$ [%] | 0.06 | 0.24 | 0.01 | 0.14 | 0.05 | 0.25 | 0.10 | 0.15 | 0.07 | 0.23 | 0.11 | 0.26 |

saturation and functional group influence the ligand's thermal stability. For both amines and carboxylic acids, the ligand's innate thermal stability ($T_{On}$, $T_I$, and $T_{Off}$) increased with the number of double bonds. Additionally, the amine ligands comparatively had lower thermal stabilities than the carboxylic acids.

In addition to contrasting temperatures of the first thermal event, mass loss percentages were also considered. Between room temperature and 500 °C, DDA, OLA, and SA underwent one thermal event, which did not produce a stable residue (wt %$_{Off}$ = ≤ 1; wt %$_{500\ °C}$ ≤ 0.05%). A different result occurred for LOA, OA, and LA; the residual material was present following $T_{Off}$. For LOA, a relatively substantial 14.5% (wt %$_{Off}$) of material remained following the ligand's first thermal event at 262 °C ($T_I$). This residual material was eliminated, following a second thermal event ($T_{II}$ = 453 °C). Similar to LOA, residue remained ensuing the first thermal events of OA (wt %$_{Off}$ = 2.9%) and LA (wt %$_{Off}$ = 8.3%) and was eliminated after a final thermal event at $T_{II}$ ≥ 429 °C.

From these variations in mass residue, trends based on bond saturation and functional group can be concluded. For both saturated amine and carboxylic acid ligands, stable carbon products did not form, indicating that external variables (i.e., precursors) must have contributed to the observed ligand decomposition during CZTS synthesis. Upon introducing a double bond along the ligand backbone, results diverged depending on the functional group: OLA (amine) experienced a similar TGA profile to that of the saturated ligands, while OA (carboxylic acid) had a small fraction of material remain. As the number of double bonds increased to two, the amount of residual material increased for both amines and carboxylic acids, with residue being more pronounced for LOA than that of LA. Therefore, ligand decomposition is correlated with the number of double bonds, whereas decomposition dependent on the functional group is variable.

As established, the origins of the observed mass loss event can result from (1) vaporization, (2) pyrolysis into volatile species, or a (3) chemical reaction. As only ligands were used and the experiment was conducted in an inert atmosphere, the probability of a chemical reaction occurring is low. However, both vaporization and pyrolysis are plausible. While the first thermal event of ligands does not appear to align with their reported boiling points ($T_{BP}$, included in Table 2), vaporization can occur at $T \neq T_{BP}$ when isothermal sample heating is

not achieved or when vapor pressure is not carefully regulated.[81] As these parameters were not controlled during our experiments, it is possible that the first thermal event could correspond to vaporization of the ligand. Alternatively, pyrolysis might have occurred. In the biofuel industry, the pyrolysis of carboxylic acids ligands has been studied. The pyrolysis of SA,[49,51,52] OA,[49−51] and LA[49,51,59] results in the formation of both volatile (e.g., CO (g) and $CO_2$ (g), short-chain hydrocarbons) and stable decomposition products (e.g., alkenes, alkanes, branched hydrocarbons, and both mono- and polyaromatics) from decarboxylation and deoxygenation of the functional group and thermal cracking of the ligand backbone.[49−52,59]

In this work, we observe that nearly 100% of SA was eliminated by $T_{Off}$, which would be in agreement with pyrolysis studies in which ~95% of SA is converted into gaseous products.[52] The presence of residue at $T_{Off}$ for OA[50] and LA[59] is also consistent with their reported pyrolysis, where a stable liquid product is formed during thermal decomposition.[50,59] The formation of these stable products for OA and LA—and lack thereof for SA—is attributed to the increased reactivity of alkenes and dienes. If pyrolysis occurs during the first thermal event, we additionally observe that saturated DDA and monounsaturated OLA do not decompose into a stable residue, while polyunsaturated LOA does. Thus, across both functional groups, double bonds contribute to the conversion of the ligand into stable decomposition products.

Regardless of the mechanism that occurred during the first thermal event, from TGA, it is evident that saturated SA and DDA and monounsaturated amine OLA did not inherently produce thermally stable carbon products. Therefore, external variables used during the synthesis of CZTS NPs (i.e., precursors) likely contributed to their in situ decomposition into carbon impurities observed in Figure 2. For ligands which produced stable products (monounsaturated OA, polyunsaturated LA, and LOA), the amount of ligand converted into residue increased with the number of double bonds, in agreement with other pyrolysis studies.

**3.3. Thermal Stability of Amine−Sulfur and Carboxylic Acid−Sulfur Mixtures.** In Section 3.2, ligand pyrolysis studies were conducted in the absence of precursors used in the synthesis of NPs to better understand how the ligand's bond saturation and functional groups influences its innate thermal stability. Interestingly, we observe a dichotomy
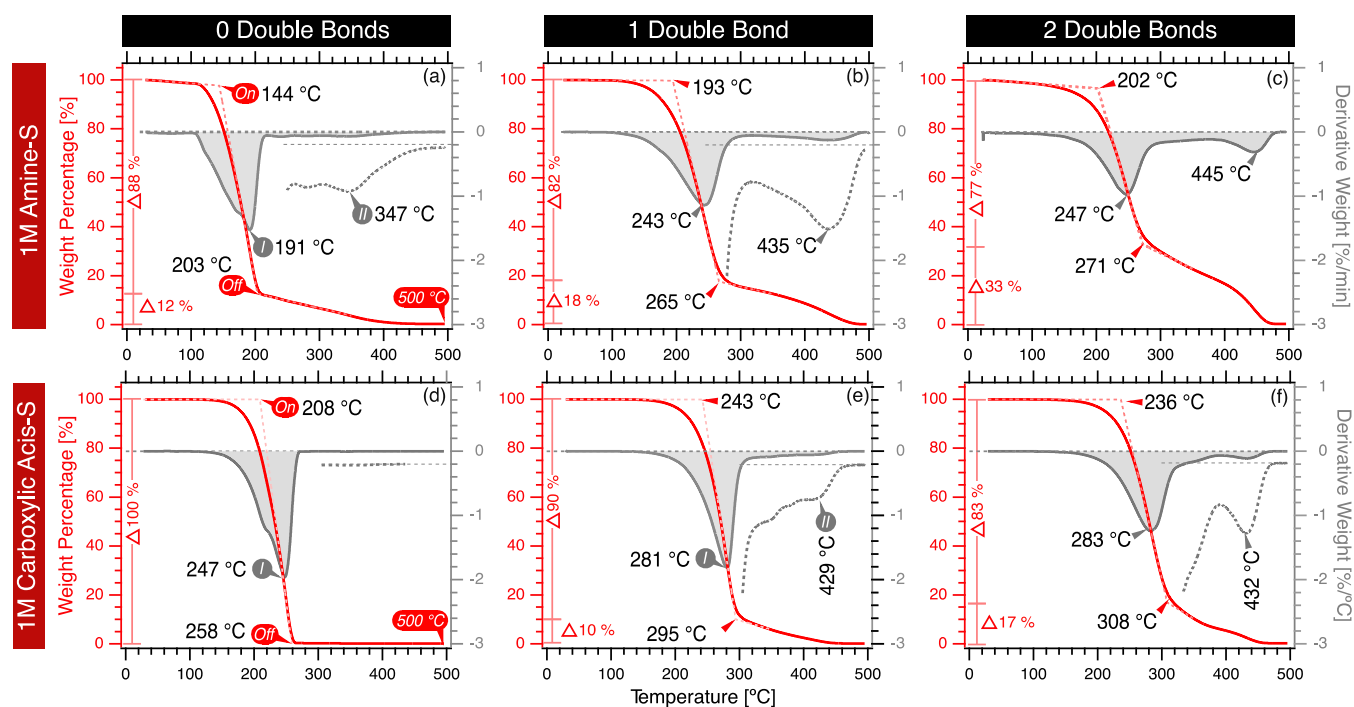
**Figure 4.** TGA (red) mass loss profiles and overlayed derived DTG (gray) curves for (a–c) 1 M amine–S and (d–f) 1 M carboxylic acid–S mixtures with varying bond saturation. This includes (a) DDA-S, (b) OLA-S, (c) LOA-S, (d) SA-S, (e) OA-S, and (f) LA-S. For clarity, the DTG signal is amplified by 10× between 250 and 500 °C (gray dashed curve). Identification of key features is performed as described in Figure 3, which contains the TGA and DTG spectra of corresponding ligands without the inclusion of elemental sulfur. All extracted values are listed in Table 2.

between NP synthesis results from Section 3.1 and isolated ligand results from Section 3.2, indicating that precursors contribute to ligand pyrolysis during synthesis.

As elemental sulfur is a common precursor used in the synthesis of chalcogenide NPs—including in the synthesis of CZTS—we additionally used TGA and DTG to compare changes between the innate ligand's thermal stability and that of 1 M ligand–sulfur mixtures (3.5–4 wt/wt % sulfur to ligand), referred to as "ligand–S". The TGA and DTG profiles of ligand–S are displayed in Figure 4 and are directly comparable to the profiles in Figure 3.

Initially, the mass loss profile of the ligand–S mixtures appears to mirror that of their innate ligand. However, there are several distinct differences upon sulfur inclusion. Between ligand and ligand–S, the maximum change in $T_I$ was, respectively, −2 and +2 °C for DDA and SA (0 double bonds), −14 and +3 °C for OLA and OA (1 double bond), and −20 and +5 °C for LOA and LA (2 double bonds). Thus, by observing the temperatures associated with the first thermal event, we see that (1) compared to amines, amine–S mixtures have a net decline in thermal stability, (2) compared to carboxylic acids, carboxylic acid–S mixtures have a net increase in thermal stability, (3) this effect is considerably more pronounced for amine–S than that of carboxylic acid–S, and (4) the difference in $T_I$ between ligand and ligand–S increases with the number of double bonds. Therefore, in the presence of elemental sulfur, amine ligands either experienced a decrease in ligand volatility, more readily pyrolyzed into volatile compounds or a chemical reaction occurred between the amine and sulfur to produce volatile compounds (the inverse would apply for carboxylic acid–S).

Changes in mass residue upon sulfur inclusion were also observed. While the heating of DDA and OLA (and SA) did not produce thermally stable carbon products, upon

completion of the first thermal event of DDA-S and OLA-S, a significant percentage (wt $\%_{Off, DDA-S}$ = 12.3%; wt $\%_{Off, OLA-S}$ = 17.6%) of material remained. Assuming that the ligand and sulfur did not react, they may have separately volatilized or pyrolyzed, evident by inflection points separately corresponding to the ligand and to elemental sulfur. While $T_I$ of ligand–S mixtures agrees with $T_I$ of their respective ligands, $T_{II}$ cannot be assigned to elemental sulfur (see Figure S4 for elemental sulfur's TGA profile). This indicates that the material present following $T_{off}$ is not residual elemental sulfur rather a ligand–S decomposition or reaction product. Unlike with DDA-S and OLA-S, the inclusion of sulfur had no effect on SA-S mass loss profile. This is notable, as the decomposition of SA was observed during the synthesis of CZTS NPs, emphasizing that variables other than elemental sulfur and ligand structure (i.e., metal precursors) must be responsible for the *in situ* decomposition of SA.

Unlike DDA, OLA, and SA ligands, in the absence of sulfur, LOA, OA, and LA ligands did produce thermally stable carbon products upon heating. Compared to LOA, LOA-S experienced a significant increase in the amount of residue from 14.5% (wt$_{Off, LOA}$) to 32.8% (wt$_{Off, LOA-S}$). The LOA-S product was fully eliminated, following a second thermal event at 445 °C ($T_{II}$). OA-S and LA-S similarly preserved a respective 10.0 and 17.0% (wt $\%_{Off}$), a relative increase compared to their innate ligand counterparts. Residual material was similarly reduced, following a second thermal event ($T_{II, OA-S}$ = 439 °C, $T_{II, LA-S}$ = 432 °C).

From these TGA and DTG results, it is apparent that the inclusion of elemental sulfur contributes to the formation of residue, and the amount of residue which forms is dependent on the ligand's innate structure. Across both amine–S and carboxylic acid–S, we observed that the wt $\%_{Off, ligand-S}$ was consistently greater than wt $\%_{Off, ligand}$. Additionally, the wt $\%_{Off}$
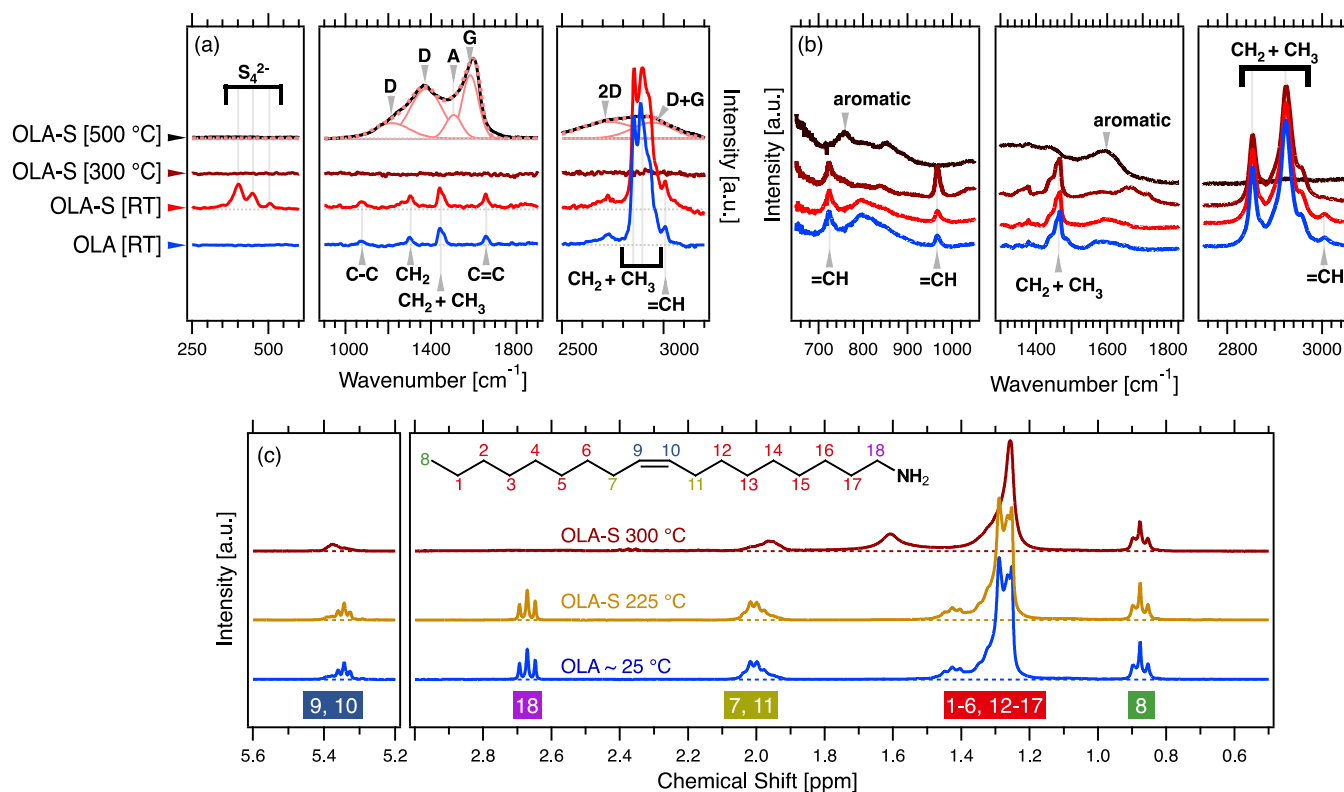
**Figure 5.** Truncated (a) Raman, (b) FTIR, and (c) $^1$H NMR of OLA and OLA-S heated at varying temperatures under $N_2$. See the supporting information for OLA-S's structure at additional temperatures (Figure S6), equivalent spectra reproduced for OA and OA-S (Figure S7), and integrated areas of $^1$H NMR signals (Table S1).

of residue consistently increased with the number of double bonds. Notably, this was considerably more pronounced for amine ligands than of carboxylic acids; there was a 11−18% increase in wt %$_{Off}$ for amine−S and a 0−9% increase in wt %$_{Off}$ for carboxylic acid−S. These results signify that (1) when compared to carboxylic acid ligands, the interaction between sulfur and amine favors the formation of stable carbon products and (2) the interaction between sulfur and double bonds contributes to the formation of stable carbon products.

Amine−S decomposition may have been more favorable than carboxylic acid−S due to the interactions between the ligand and sulfur. Sulfur is known to undergo a ring-opening reaction facilitated by nucleophilic amines, transforming cyclic $S_8$ into anionic linear sulfur chains, which then further react with the ligand to produce volatile $H_2S$ (g) and thioamides, amidine oligomers, or alkylammonium polysulfides of different thermal stabilities.[34,38,82,83] This may be why amine−S exhibited a decrease in $T_{On}$ (release of volatile reaction products) and an increase in wt %$_{Off}$ (formation of stable reaction products). In contrast, carboxylic acids do not favorably undergo nucleophilic ring-opening with elemental sulfur; thus, additives are commonly used to enhance miscibility and to catalyze chemical reactions to form C−S bonds.[56,58,84] This is reflected in our observations of dissolving sulfur in the ligands (see Section 2.2). The poor miscibility and reactivity between carboxylic acids and sulfur may be why both critical temperatures and residual mass upon sulfur inclusion were dampened compared to amines.

The increased residue for ligands with double bonds is likely attributed to enhanced degree of polymerization and aromatization alkenes—and even more so—dienes can undergo due to the heightened reactivity of double bonds.

As previously discussed, the pyrolysis of innate ligands with double bonds has been reported to result in the formation of stable products, including alkenes, alkanes, branched hydrocarbons, and both mono- and polyaromatics.[49−52,59] With the inclusion of elemental sulfur, additional reactions may transpire. Alkenes, which specifically include OLA, OA, and LA, have previously been reported to be polymerized by ionic sulfur via a reaction referred to as inverse vulcanization.[34,38,58,79] This mechanism involves the cross-linking of unsaturated ligands at their allylic sites by ionic linear sulfur chains to form polysulfides.[34,38,79] As the number of double bonds increases, so does the potential molecular weight and thus thermal stability of the products. This is reflected in our TGA results; as the number of double bonds increased, the $T_{II}$ (thus, thermal stability) of the residual material also increased, which may be attributed to an increase in the molecular weight or bond energies of reaction products. The amount of material converted into a stable product also increased with the number of double bonds, again indicating a trend between bond saturation and reactivity.

By these observations, it is feasible that the material remaining between $T_{Off}$ and $T_{II}$ is comprised of stable reaction products (oligomers, polysulfides), which may be precursors to the alkylated graphitic products detected after NP synthesis. Alternatively, the present products may already contain alkylated graphitic products following pyrolysis. As TGA does not provide structural information, we used Raman spectroscopy, FTIR, and $^1$H NMR to identify the material at $T_I$ < T < $T_{II}$ (see Figures 5, S6 and S7).

At room temperature, signature $CH_2$, $CH_3$, C−C, C=C, and =CH bonding modes of OLA were detected via Raman and FTIR.[61,85] Upon mixing OLA with sulfur, we did not

detect Raman bands associated with elemental sulfur (see Figure S4). Rather, the emergence of peaks at 403, 447, and 505 cm$^{-1}$ was identified, which correspond with ionic sulfur ($S_4^{2-}$), in agreement with the ring opening of elemental sulfur by the ligand's amine group.[33,86,87]

With increased heating of OLA-S, the Raman spectrum showed signs of fluorescence and was no longer well resolved.[33] This arises from the formation of fluorescent materials, such as polysulfides or carbon dots.[54,61,88] As we could not elucidate structural information from Raman, both FTIR and $^1$H NMR were important supplements. From 130−225 °C, there were no notable changes in OLA's structure. However, at 300 °C ($T_I < T_{300 °C} < T_{II}$), we began to see degradation of the double bond; there was a decline in $=CH$ (FTIR, at 3010 cm$^{-1}$) and a decline in allylic and vinylic hydrogen bonding ($^1$H NMR, at ~5.2 and 2.0 ppm, respectively). $^1$H NMR additionally shows an 81% reduction of the signal associated with the ligand's $\alpha$ carbon ($C\alpha$), indicating a reaction with or decomposition of the amine functional group occurred. As the original hydrocarbon structure remains intact at 300 °C and degradation is only observed at the double bond and functional group, the residual material's structure is most consistent with that of a polysulfide.[34] Following the decomposition of the stable polysulfide at $T_{II}$, Raman spectra of the material are again discernable ($T_{500 °C}$); notably, we see the presence of the D$_4$-, D-, A-, and G-bands, and no bands associated with the starting ligand. At $T_{500 °C}$, FTIR also shows an elimination of hydrocarbon peaks, with a spectrum that is representative of early-stage soot formation.[75]

Similar results were found for OA-S (see Figure S7). From FTIR, the dominant change in the structure of carboxylic acid−S includes attenuation of $=CH$ and the functional group's C=O signal (1709−1720 cm$^{-1}$). The changes in $^1$H NMR mirror that of amine−S; at $T_{300 °C}$, the most significant spectral changes were intensity reductions in allylic and vinyl sites. There was also a 24% reduction in intensity of the $C\alpha$ signal, relatively less of a change within the ligand's functional group compared to amines.

These structural changes are consistent with decomposition at the double bond sites and of functional groups into a polysulfide[50,52,59] rather than the conversion of ligand−S into alkylated graphitic impurities via pyrolysis.[89] However, above $T_{II}$ (>347 °C), we confirmed that these products carbonized into the same alkylated graphitic product detected after NP synthesis at 225 °C. As graphitic carbon was detected within CZTS NPs synthesized with both amines and carboxylic acids, it appears that the introduction of metallic precursors contributes to the in situ ligand pyrolysis at temperatures below $T_{II}$.

## 3.4. Precursor Selection-Dependent Pyrolysis of Oleylamine during NP Synthesis.

Thus far, alkylated graphitic carbon has been detected during the synthesis of CZTS NPs at 225 °C. In the absence of metal precursors, we observe that both amine and carboxylic acid ligands can form stable carbon products. Despite graphitic carbon being detected in all CZTS samples, the extent and tendency of ligands to innately decompose are dependent on bond saturation and functional group. Additionally, decomposition into graphitic material occurs at temperatures that exceed our synthesis conditions. This indicates that metal precursors—the final variables introduced in the synthesis of CZTS NPs—contribute to the in situ decomposition of ligands.

To fully decouple the influence of metal precursors on ligand decomposition, the copper-, zinc-, and tin-based acetylacetonate ($(acac)_2$) precursors were separately heated with the OLA ligand in both the absence and presence of elemental sulfur. While it would be ideal to avoid the formation of NPs during these experiments, heating the ligand with the metal precursors at 225 °C favorably resulted in metal/metal oxide NPs (sulfur-free conditions) and metal-chalcogenide NPs (sulfur-containing conditions). Table 3 includes the full list of samples and

**Table 3. Reactants and Products from Synthesized NP Samples**

| sample | reactants | inorganic products |
|---|---|---|
| Cu NPs | OLA, Cu(acac)$_2$ | Cu, CuO, Cu$_2$O |
| Cu−S NPs | OLA, Cu(acac)$_2$, S | CuS, Cu$_{1.8}$S |
| Zn NPs | OLA, Zn(acac)$_2$ | ZnO |
| Zn−S NPs | OLA, Zn(acac)$_2$, S | ZnS, ZnO |
| Sn NPs | OLA, SnBr$_2$(acac)$_2$ | Amorphous Sn |
| Sn−S NPs | OLA, SnBr$_2$ (acac)$_2$, S | SnS, Sn |

their resulting NP phases, and Figure S8 contains the structural confirmation of identified materials via Raman spectroscopy and XRD. Here, OLA was selected as the standard ligand since TGA results reveal that this ligand is relatively benign in absence of all precursors but is still capable of complex decomposition when pyrolyzed in the presence of elemental sulfur.

Akin to that of the CZTS NPs and the pyrolyzed TGA residue, we identified the structure of organic products within the region between 1000−1800 cm$^{-1}$, as emphasized in Figure 6. Both Zn−S and Sn NP Raman signals were oversaturated with high fluorescence, suppressing all distinct signals and making these materials ineligible for further carbon-based analyses.

Cu NPs synthesized with OLA resulted in a weak broad peak centered at 1568 cm$^{-1}$, fitted in Figure 6. The peak position would align with a G-band assignment, indicating that there was a graphitic structure. However, no other assignments from Table 1 were distinguishable in the Cu NP's Raman spectra. As the graphitic material becomes increasingly amorphous, the G-band further broadens and the D-band becomes indistinguishable,[85] which resembles our Cu NP Raman spectra. Zn NPs even more so did not share the same carbon structure identified from CZTS synthesis, with no graphitic or amorphous bands being detectable. Rather, detected bands can be assigned to the Raman spectra of OLA (see Figure S5). This includes the C−C bonding (1058 and 1124 cm$^{-1}$) and OLA's highest intensity of CH$_2$ and CH$_3$ scattering modes between 2830 and 2925 cm$^{-1}$.[66]

Unlike the sulfur-free syntheses, the carbon impurity present from CZTS synthesis appears to be found in Cu−S and Sn−S NP samples. In Cu−S NPs, Raman signals associated with the structured G- and D-bands, the defective/amorphous D$_4$- and A-bands, an unidentified band at 1431 cm$^{-1}$, and second-order graphitic bands were all identified. When directly compared to the products from Cu NP synthesis, it is evident that the inclusion of elemental sulfur led to the formation of carbon impurities with a structure more similar to that of CZTS, which has a more graphitic structure. Akin to Cu−S, Sn−S NPs had formed structured carbon, with the G-, D-, D$_4$-, and second-order bands being detected. Fitting of the A-band and
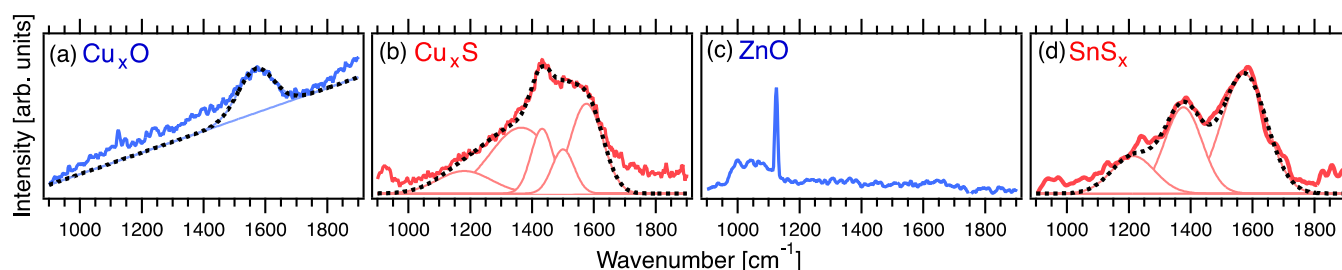
**Figure 6.** Raman spectra for NPs synthesized with (a, b) Cu(acac)$_2$, (c) Zn(acac)$_2$, and (d) SnBr$_2$(acac)$_2$ organometallic precursors, all labeled by their resulting formed NPs. The peak centers of carbon-based modes are labeled and deconvoluted with Gaussian fits, if possible. Full structural analysis of each NP (Raman and XRD) is found in supplemental Figure S8. The relative intensities are not comparable, and no background subtraction was used CuO$_x$ spectra rather a linear background fit between 900 and 1900 cm$^{-1}$ is included with the spectra.

unassigned band from 1427−1439 cm$^{-1}$ was not necessary to deconvolute the Sn−S NP carbon signal.

In summary, Raman revealed that the sulfur-based synthesis of Cu−S and Sn−S led to the formation of carbon impurities, which are structurally similar to the carbon impurities found in CZTS samples. The Cu NP sample also formed carbon residue but with a more amorphous structure. Zn was the only NP sample to have the original ligand's structure (OLA) detectable after synthesis and no indication of decomposed carbon products. This means that the OLA remained stable at 225 °C when heated with Zn(acac)$_2$, whereas the ligand decomposed when exposed to Cu(acac)$_2$ and SnBr$_2$(acac)$_2$ precursors and their synthesized NPs.

Both metal precursors and the formed NPs have been used in catalysis. M-(acac)$_2$ precursors are versatile catalysts, which participates in a wide library of low-temperature organic reactions, which includes oligomerization, polymerization, and polycondensation, hydrogenation, isomerization, trans-esterification, and can also be used as catalysts in reactions between sulfur and organic monomers, including inverse vulcanization.[42,90−94] Additionally, all of our formed NPs (CZTS, Cu, CuO, Cu$_2$O, Cu$_x$S, ZnO, ZnS, Sn, and SnS) are either chemically, photochemically, or electrochemically catalytic and can catalyze the reactions with or the degradation of organic materials.[95−100] As such, it is possible that the metal precursors or the formed NPs are catalytically promoting ligand decomposition at 225 °C.

To our knowledge, reactions facilitated by Cu, Zn, and Sn catalysts do not extensively include the aromatization and graphitization of organic materials. However, metal foils (including Cu) have been used as catalysts in the production of graphene sheets from organic monomers.[101]

These results raise additional questions, which are open for further study, such as the mechanism guiding how the precursors or the formed NPs may catalyze ligand decomposition. Additionally, factors such as reaction time and temperature may also modulate ligand decomposition by impacting reaction kinetics. Tailoring precursor selection, reaction time, and reaction temperature may assist in mitigating or controlling in situ ligand decomposition.[13,24]

## ■ CONCLUSIONS

Recent works have revealed that organic ligands used in the synthesis of inorganic nanoparticles are capable of thermally decomposing into polymeric and graphitic impurities during synthesis. However, no systematic studies have been conducted to determine how internal variables innate to the ligand (i.e., functional group and bond saturation) and external

variables used in NP synthesis (i.e., metal and nonmetal precursors) influence ligand decomposition.

In this work, we use a combination of thermal analyses (TGA) and structural analyses (Raman spectroscopy, FTIR, and $^1$H NMR) to identify the origins of this complex in situ ligand decomposition. Here, we investigate (1) the decomposition of ligands with varying functional groups (amines and carboxylic acids) and bond saturation (fully saturated to polyunsaturated) and (2) the direct influence that external variables (i.e., elemental sulfur, Cu acetylacetonate, Zn acetylacetonate, and Sn acetylacetonate) individually have on ligand decomposition.

In both the presence and absence of external variables, we found that bond saturation was universally a determining factor for decomposition, where the number of double bonds correlated directly with ligand polymerization or pyrolysis. When contrasting amine and carboxylic acid functional groups, differences in decomposition were dependent on external variables; comparatively amines formed more byproducts (polysulfides) in the presence of elemental sulfur, whereas carboxylic acids had produced higher concentrations of byproducts (alkylated graphitic carbon) upon the addition of metal precursors (i.e., during the synthesis of CZTS NPs).

Regardless of bond saturation or functional group, decomposition was less substantial when in the absence of precursor materials, emphasizing how ligand decomposition during NP synthesis primarily results from external variables. When synthesizing CZTS, Cu$_x$O, Cu$_x$S, ZnO, ZnS, SnS$_x$, and SnO$_x$ NPs, we additionally unveil the individual influence that nonmetal and metal precursor selection has on in situ ligand decomposition. Notably, the formation of alkylated graphitic impurities was identified in the synthesis of chalcogenides (CZTS, Cu$_x$S, and SnS$_x$), whereas lesser decomposition was observed when only the Cu precursor was used (Cu$_x$O), and no decomposition occurred with only the Zn precursor (ZnO).

Decoupling variables, which lead to ligand decomposition during NP synthesis, is an important step toward reducing or controlling the formation of byproducts. Future studies can focus on synthesis conditions (i.e., time, temperature), investigating decomposition within the wide library of ligands (e.g., thiols, hydroxyls, phosphines and phosphine oxides, polymers, proteins), sulfur precursors (e.g., thiols, thiourea, thiosulfates, thiolates, thiocarbamates), other chalcogenide precursors (e.g., elemental selenium, selenium oxides, selenourea, elemental tellurium, alkyl tellurides, chalcogenide-based metal−organic precursors), and metal precursors (e.g., acetates, nitrates, halides, carbonyls, sulfates) used in NP synthesis.[3,102−104]

## ASSOCIATED CONTENT

### Supporting Information

The Supporting Information is available free of charge at https://pubs.acs.org/doi/10.1021/acs.chemmater.2c03006.

> Procedure for the synthesis of LOA and corresponding H$^1$ NMR; additional methods for individual NP synthesis; TGA and Raman spectra of purified OLA, experiments repeated with ODA, and of elemental sulfur; Raman and FTIR spectra of OLA-S and OA-S; $^1$H NMR of OLA-S and OA-S; and XRD and Raman spectra of Cu, Cu-S, Zn, Zn-S, Sn, and Sn-S NPs (PDF)

## AUTHOR INFORMATION

### Corresponding Author

**Christine K. Luscombe** − *Department of Materials Science and Engineering, University of Washington, Seattle, Washington 98195, United States; Department of Chemistry, University of Washington, Seattle, Washington 98195, United States; Pi-Conjugated Polymers Unit, Okinawa Institute of Science and Technology, Okinawa 904-0495, Japan;* orcid.org/0000-0001-7456-1343; Email: christine.luscombe@oist.jp

### Authors

**Breena M. Sperry** − *Department of Materials Science and Engineering, University of Washington, Seattle, Washington 98195, United States;* orcid.org/0000-0003-2462-8276

**Nadzeya A. Kukhta** − *Department of Chemistry, University of Washington, Seattle, Washington 98195, United States*

**Yunping Huang** − *Department of Materials Science and Engineering, University of Washington, Seattle, Washington 98195, United States; University of Colorado Boulder, Boulder, Colorado 80309, United States;* orcid.org/0000-0001-8461-7160

Complete contact information is available at:
https://pubs.acs.org/10.1021/acs.chemmater.2c03006

### Author Contributions

B.M.S. carried out conceptualization, experimental design, nanomaterials synthesis, characterization, analysis, and writing for this manuscript. N.A.K. collected $^1$H NMR. Y.H. synthesized a commercially unavailable ligand (LOA) used in this study. C.K.L. supervised all stages of this study. All authors have given approval to the final version of the manuscript.

### Notes

The authors declare no competing financial interest.

## ACKNOWLEDGMENTS

## ABBREVIATIONS USED

DTG, derivative thermogravimetry; DDA, dodecylamine; FTIR, Fourier transform infrared spectroscopy; LA, linoleic acid; LOA, linoleylamine; NP(s), nanoparticle(s); OA, oleic acid; OLA, oleylamine; SA, stearic acid; XRD, X-ray diffraction

## REFERENCES

(1) Ealias, A. M.; Saravanakumar, M. P. A Review on the Classification, Characterisation, Synthesis of Nanoparticles and Their Application. *IOP Conf. Ser.: Mater. Sci. Eng.* **2017**, *263*, No. 032019.

(2) Ali, A.; Shah, T.; Ullah, R.; Zhou, P.; Guo, M.; Ovais, M.; Tan, Z.; Rui, Y. Review on Recent Progress in Magnetic Nanoparticles: Synthesis, Characterization, and Diverse Applications. *Front. Chem.* **2021**, *9*, No. 629054.

(3) Heuer-Jungemann, A.; Feliu, N.; Bakaimi, I.; Hamaly, M.; Alkilany, A.; Chakraborty, I.; Masood, A.; Casula, M. F.; Kostopoulou, A.; Oh, E.; Susumu, K.; Stewart, M. H.; Medintz, I. L.; Stratakis, E.; Parak, W. J.; Kanaras, A. G. The Role of Ligands in the Chemical Synthesis and Applications of Inorganic Nanoparticles. *Chem. Rev.* **2019**, *119*, 4819−4880.

(4) Salata, O. Applications of Nanoparticles in Biology and Medicine. *J. Nanobiotechnol.* **2004**, *2*, 3.

(5) Luo, X.; Morrin, A.; Killard, A. J.; Smyth, M. R. Application of Nanoparticles in Electrochemical Sensors and Biosensors. *Electroanalysis* **2006**, *18*, 319−326.

(6) Matsui, I. Nanoparticles for Electronic Device Applications: A Brief Review. *J. Chem. Eng. Japan* **2005**, *38*, 535−546.

(7) Choi, J.-r.; Shin, D.-M.; Song, H.; Lee, D.; Kim, K. Current Achievements of Nanoparticle Applications in Developing Optical Sensing and Imaging Techniques. *Nano Converg.* **2016**, *3*, No. 30.

(8) Narayan, N.; Meiyazhagan, A.; Vajtai, R. Metal Nanoparticles as Green Catalysts. *Materials* **2019**, *12*, 3602.

(9) An, L.; Zhang, D.; Zhang, L.; Feng, G. Effect of Nanoparticle Size on the Mechanical Properties of Nanoparticle Assemblies. *Nanoscale* **2019**, *11*, 9563−9573.

(10) Albanese, A.; Tang, P. S.; Chan, W. C. W. The Effect of Nanoparticle Size, Shape, and Surface Chemistry on Biological Systems. *Annu. Rev. Biomed. Eng.* **2012**, *14*, 1−16.

(11) Saion, E.; Gharibshahi, E.; Naghavi, K. Size-Controlled and Optical Properties of Monodispersed Silver Nanoparticles Synthesized by the Radiolytic Reduction Method. *Int. J. Mol. Sci.* **2013**, *14*, 7880−7896.

(12) Ijaz, P.; Imran, M.; Soares, M. M.; Tolentino, H. C. N.; Martín-García, B.; Giannini, C.; Moreels, I.; Manna, L.; Krahne, R. Composition-, Size-, and Surface Functionalization-Dependent Optical Properties of Lead Bromide Perovskite Nanocrystals. *J. Phys. Chem. Lett.* **2020**, *11*, 2079−2085.

(13) Li, S.; Chen, J.; Ying Tang, Y.; Yu Hu, L.; Hui Qian, W.; Zhu, D.; Chen, P. Green Synthesis of Upconversion Nanocrystals by Adjusting Local Precursor Supersaturation under Aqueous Conditions. *Mater. Adv.* **2020**, *1*, 2707−2711.

(14) Arno, M. C.; Inam, M.; Weems, A. C.; Li, Z.; Binch, A. L. A.; Platt, C. I.; Richardson, S. M.; Hoyland, J. A.; Dove, A. P.; O'Reilly, R. K. Exploiting the Role of Nanoparticle Shape in Enhancing Hydrogel Adhesive and Mechanical Properties. *Nat. Commun.* **2020**, *11*, No. 1420.

(15) Singh, A.; Lutz, L.; Ong, G. K.; Bustillo, K.; Raoux, S.; Jordan-Sweet, J. L.; Milliron, D. J. Controlling Morphology in Polycrystalline Films by Nucleation and Growth from Metastable Nanocrystals. *Nano Lett.* **2018**, *18*, 5530−5537.

(16) Collord, A. D.; Hillhouse, H. W. Mapping the Composition Dependence of Cu$_2$ZnSn(S,Se)$_4$ Absorber Quality Using Composition-Spread Libraries, Photoluminescence, and Raman. *Conf. Rec. IEEE Photovolt. Spec. Conf.* **2013**, 368−370.

(17) Irkhina, A.; Levcenko, S.; Hinrichs, V.; Plate, P.; Unold, T. Metal Acetate Based Synthesis of Small-Sized Cu$_2$ZnSnS$_4$ Nanocrystals: Effect of Injection Temperature and Synthesis Time. *RSC Adv.* **2017**, *7*, 11752−11760.

(18) Just, J.; Sutter-Fella, C. M.; Lützenkirchen-Hecht, D.; Frahm, R.; Schorr, S.; Unold, T. Secondary Phases and Their Influence on the

Composition of the Kesterite Phase in CZTS and CZTSe Thin Films. *Phys. Chem. Chem. Phys.* **2016**, *18*, 15988−15994.

(19) Thanh, N. T. K.; Maclean, N.; Mahiddine, S. Mechanisms of Nucleation and Growth of Nanoparticles in Solution. *Chem. Rev.* **2014**, *114*, 7610−7630.

(20) Boles, M. A.; Ling, D.; Hyeon, T.; Talapin, D. V. The Surface Science of Nanocrystals. *Nat. Mater.* **2016**, *15*, 141−153.

(21) Huang, Y.; Cohen, T. A.; Sperry, B. M.; Larson, H.; Nguyen, H. A.; Homer, M. K.; Dou, F. Y.; Jacoby, L. M.; Cossairt, B. M.; Gamelin, D. R.; Luscombe, C. K. Organic Building Blocks at Inorganic Nanomaterial Interfaces. *Mater. Horiz.* **2022**, *9*, 61−87.

(22) Mourdikoudis, S.; Liz-Marzán, L. M. Oleylamine in Nanoparticle Synthesis. *Chem. Mater.* **2013**, *25*, 1465−1476.

(23) Wang, W.; Banerjee, S.; Jia, S.; Steigerwald, M. L.; Herman, I. P. Ligand Control of Growth, Morphology, and Capping Structure of Colloidal CdSe Nanorods. *Chem. Mater.* **2007**, *19*, 2573−2580.

(24) Yu, W. W.; Wang, Y. A.; Peng, X. Formation and Stability of Size-, Shape-, and Structure-Controlled CdTe Nanocrystals: Ligand Effects on Monomers and Nanocrystals. *Chem. Mater.* **2003**, *15*, 4300−4308.

(25) Grubbs, R. B. Roles of Polymer Ligands in Nanoparticle Stabilization. *Polym. Rev.* **2007**, *47*, 197−215.

(26) Peters, J. L.; Van Den Bos, K. H. W.; Aert, S. V.; Goris, B.; Bals, S.; Vanmaekelbergh, D. L. Ligand-Induced Shape Transformation of PbSe Nanocrystals. *Chem. Mater.* **2017**, *29*, 4122−4128.

(27) Dhaene, E.; Billet, J.; Bennett, E.; Driessche, I. V.; De Roo, J. The Trouble with ODE: Polymerization during Nanocrystal Synthesis. *Nano Lett.* **2019**, *19*, 7411−7417.

(28) Sperry, B. M.; Luscombe, C. K. Ligand Pyrolysis during Air-Free Inorganic Nanocrystal Synthesis. *Chem. Mater.* **2021**, *33*, 136−145.

(29) Calcabrini, M.; Van den Eynden, D.; Ribot, S. S.; Pokratath, R.; Llorca, J.; De Roo, J.; Ibáñez, M. Ligand Conversion in Nanocrystal Synthesis: The Oxidation of Alkylamines to Fatty Acids by Nitrate. *JACS Au* **2021**, *1*, 1898−1903.

(30) De Keukeleere, K.; Coucke, S.; De Canck, E.; Van Der Voort, P.; Delpech, F.; Coppel, Y.; Hens, Z.; Van Driessche, I.; Owen, J. S.; De Roo, J. Stabilization of Colloidal Ti, Zr, and Hf Oxide Nanocrystals by Protonated Tri- *n* -Octylphosphine Oxide (TOPO) and Its Decomposition Products. *Chem. Mater.* **2017**, *29*, 10233−10242.

(31) Wolcott, A.; Fitzmorris, R. C.; Muzaffery, O.; Zhang, J. Z. CdSe Quantum Rod Formation Aided By In Situ TOPO Oxidation. *Chem. Mater.* **2010**, *22*, 2814−2821.

(32) Kim, E. T.; Chung, W. J.; Lim, J.; Johe, P.; Glass, R. S.; Pyun, J.; Char, K. One-Pot Synthesis of PbS NP/Sulfur-Oleylamine Copolymer Nanocomposites via the Copolymerization of Elemental Sulfur with Oleylamine. *Polym. Chem.* **2014**, *5*, 3617−3623.

(33) Lynch, M. An Investigation of Solutions of Sulfur in Oleylamine by Raman Spectroscopy and Their Relation to Lead Sulfide Quantum Dot Synthesis. Undergraduate Honors Theses. Undergraduate Honors Theses; University of Colorado: Boulder, USA, 2017.

(34) Thomson, J. W.; Nagashima, K.; MacDonald, P. M.; Ozin, G. A. From Sulfur-Amine Solutions to Metal Sulfide Nanocrystals: Peering into the Oleylamine-Sulfur Black Box. *J. Am. Chem. Soc.* **2011**, *133*, 5036−5041.

(35) Reiss, P.; Carrière, M.; Lincheneau, C.; Vaure, L.; Tamang, S. Synthesis of Semiconductor Nanocrystals, Focusing on Nontoxic and Earth-Abundant Materials. *Chem. Rev.* **2016**, *116*, 10731−10819.

(36) Griebel, J. J.; Glass, R. S.; Char, K.; Pyun, J. *Polymerizations with Elemental Sulfur: A Novel Route to High Sulfur Content Polymers for Sustainability, Energy and Defense*; Elsevier Ltd., 2016; Vol. *58* DOI: 10.1016/j.progpolymsci.2016.04.003.

(37) Worthington, M. J. H.; Kucera, R. L.; Chalker, J. M. Green Chemistry and Polymers Made from Sulfur. *Green Chem.* **2017**, *19*, 2748−2761.

(38) Chung, W. J.; Griebel, J. J.; Kim, E. T.; Yoon, H.; Simmonds, A. G.; Ji, H. J.; Dirlam, P. T.; Glass, R. S.; Wie, J. J.; Nguyen, N. A.; Guralnick, B. W.; Park, J.; Somogyi, A.; Theato, P.; Mackay, M. E.;

Sung, Y.-E.; Char, K.; Pyun, J. The Use of Elemental Sulfur as an Alternative Feedstock for Polymeric Materials. *Nat. Chem.* **2013**, *5*, 518−524.

(39) Wręczycki, J.; Bieliński, D. M.; Anyszka, R. Sulfur/Organic Copolymers as Curing Agents for Rubber. *Polymers* **2018**, *10*, No. E870.

(40) Brüll, R.; Kgosane, D.; Neveling, A.; Pasch, H.; Raubenheimer, H. G.; Sanderson, R.; Wahner, U. M. Synthesis and Properties of Poly-1-Olefins. *Macromol. Symp.* **2001**, *165*, 11−18.

(41) Quijada, R.; Guevara, J. L.; Yazdani-Pedram, M.; Galland, G. B.; Ribeiro, D. Study of the Polymerization of 1-Octadecene with Different Metallocene Catalysts. *Polym. Bull.* **2002**, *49*, 273−280.

(42) Kissin, Y. Chemistry and Sterochemistry of Polymerization and Copolymerization Reactions with Transition Metal Catalysts. In *Alkene Polymerization Reactions with Transition Metal Catalysts*; Elsevier, 2008; pp 1−28, pp 65−190.

(43) Shamiri, A.; Chakrabarti, M. H.; Jahan, S.; Hussain, M. A.; Kaminsky, W.; Aravind, P. V.; Yehye, W. A. The Influence of Ziegler-Natta and Metallocene Catalysts on Polyolefin Structure, Properties, and Processing Ability. *Materials* **2014**, *7*, 5069−5108.

(44) Walsh, D. J.; Hyatt, M. G.; Miller, S. A.; Guironnet, D. Recent Trends in Catalytic Polymerizations. *ACS Catal.* **2019**, *9*, 11153−11188.

(45) Erman, B.; Mark, J. E.; Roland, M. C. Chapter 7 - Vulcanization. In *Science and Technology of Rubber*; Elsevier, 2013; pp 337−381.

(46) Sandler, S. R.; Karo, W. Chapter 3 - Sulfide Polymers. In *Polymer Syntheses*; Elsevier Inc., 1996; Vol. 3, pp 73−119.

(47) Sen, M. Y. Synthesis of Middle-Chain Carboxyl- and Primary Amine-Functionalized Polystyrenes Using Anionic Polymerization Techniques. Master of Science Thesis; The University of Akron: USA, 2005.

(48) Xia, C.; Zhu, S.; Feng, T.; Yang, M.; Yang, B. Evolution and Synthesis of Carbon Dots: From Carbon Dots to Carbonized Polymer Dots. *Adv. Sci.* **2019**, *6*, No. 1901316.

(49) Kubátová, A.; Šávová, J.; Seames, W. S.; Luo, Y.; Sadrameli, S. M.; Linnen, M. J.; Baglayeva, G. V.; Smoliakova, I. P.; Kozliak, E. I. Triacylglyceride Thermal Cracking: Pathways to Cyclic Hydrocarbons. *Energy Fuels* **2012**, *26*, 672−685.

(50) Asomaning, J.; Mussone, P.; Bressler, D. C. Thermal Deoxygenation and Pyrolysis of Oleic Acid. *J. Anal. Appl. Pyrolysis* **2014**, *105*, 1−7.

(51) Idem, R. O.; Katikaneni, S. P. R.; Bakhshi, N. N. Thermal Cracking of Canola Oil: Reaction Products in the Presence and Absence of Steam. *Energy Fuels* **1996**, *10*, 1150−1162.

(52) Maher, K. D.; Kirkwood, K. M.; Gray, M. R.; Bressler, D. C. Pyrolytic Decarboxylation and Cracking of Stearic Acid. *Ind. Eng. Chem. Res.* **2008**, *47*, 5328−5336.

(53) Bourlinos, A. B.; Stassinopoulos, A.; Anglos, D.; Zboril, R.; Karakassides, M.; Giannelis, E. P. Surface Functionalized Carbogenic Quantum Dots. *Small* **2008**, *4*, 455−458.

(54) Rimal, V.; Shishodia, S.; Srivastava, P. K. Novel Synthesis of High-Thermal Stability Carbon Dots and Nanocomposites from Oleic Acid as an Organic Substrate. *Appl. Nanosci.* **2020**, *10*, 455−464.

(55) Jiang, K.; Sun, S.; Zhang, L.; Lu, Y.; Wu, A.; Cai, C.; Lin, H. Red, Green, and Blue Luminescence by Carbon Dots: Full-Color Emission Tuning and Multicolor Cellular Imaging. *Angew. Chem., Int. Ed.* **2015**, *54*, 5360−5363.

(56) Smith, A. D.; Thiounn, T.; Lyles, E. W.; Kibler, E. K.; Smith, R. C.; Tennyson, A. G. Combining Agriculture and Energy Industry Waste Products to Yield Recyclable, Thermally Healable Copolymers of Elemental Sulfur and Oleic Acid. *J. Polym. Sci.* **2019**, *57*, 1704−1710.

(57) Smith, A. D.; Tennyson, A. G.; Smith, R. C. Sulfur-Containing Polymers Prepared from Fatty Acid-Derived Monomers: Application of Atom-Economical Thiol-Ene/Thiol-Yne Click Reactions and Inverse Vulcanization Strategies. *ACS Sustainable Chem.* **2020**, *1*, 209−237.

(58) Smith, A. D.; McMillen, C. D.; Smith, R. C.; Tennyson, A. G. Copolymers by Inverse Vulcanization of Sulfur with Pure or Technical-Grade Unsaturated Fatty Acids. *J. Polym. Sci.* **2020**, *58*, 438−445.

(59) Asomaning, J.; Mussone, P.; Bressler, D. C. Pyrolysis of Polyunsaturated Fatty Acids. *Fuel Process. Technol.* **2014**, *120*, 89−95.

(60) Niu, S.; Zhou, Y.; Yu, H.; Lu, C.; Han, K. Investigation on Thermal Degradation Properties of Oleic Acid and Its Methyl and Ethyl Esters through TG-FTIR. *Energy Convers. Manage.* **2017**, *149*, 495−504.

(61) Baranov, D.; Lynch, M. J.; Curtis, A. C.; Carollo, A. R.; Douglass, C. R.; Mateo-Tejada, A. M.; Jonas, D. M. Purification of Oleylamine for Materials Synthesis and Spectroscopic Diagnostics for Trans Isomers. *Chem. Mater.* **2019**, *31*, 1223−1230.

(62) Martin, T. R.; Katahara, J. K.; Bucherl, C. N.; Krueger, B. W.; Hillhouse, H. W.; Luscombe, C. K. Nanoparticle Ligands and Pyrolized Graphitic Carbon in CZTSSe Photovoltaic Devices. *Chem. Mater.* **2016**, *28*, 135−145.

(63) Standard ASTM E2550-21. Standard Test Method for Thermal Stability by Thermogravimetry. *ASTM International*, 2021, https://www.astm.org/e2550-21.htm (accessed June 24, 2022).

(64) Standard ASTM E1131-20. Standard Test Method for Compositional Analysis by Thermogravimetry. *ASTM International*, 2020, https://www.astm.org/e1131-20.html(accessed June 24, 2022).

(65) ISO 11358-1:2014(E); E); International Standard ISO 11358-1:2014(E). Plastics — Thermogravimetry (TG) of Polymers. *International Organization for Standardization*, 2014, https://www.iso.org/standard/59710.html (accessed June 28, 2022).

(66) Larkin, P. *Infrared and Raman Spectroscopy: Principles and Spectral Interpretation*, 1st ed.; Elsevier, 2011. DOI: 10.1016/B978-0-12-386984-5.10001-1.

(67) Pelletier, M. J. Quantitative Analysis Using Raman Spectrometry. *Appl. Spectrosc.* **2003**, *57*, 20A−42A.

(68) Ferrari, A. C. Raman Spectroscopy of Graphene and Graphite: Disorder, Electron-Phonon Coupling, Doping and Nonadiabatic Effects. *Solid State Commun.* **2007**, *143*, 47−57.

(69) Castiglioni, C.; Mapelli, C.; Negri, F.; Zerbi, G. Origin of the D Line in the Raman Spectrum of Graphite: A Study Based on Raman Frequencies and Intensities of Polycyclic Aromatic Hydrocarbon Molecules. *J. Chem. Phys.* **2001**, *114*, 963−974.

(70) Childres, I.; Jauregui, L. A.; Park, W.; Cao, H.; Chen, Y. P. Raman Spectroscopy of Graphene and Related Materials. In *New developments in photon and materials research*; Nova Science Publishers: Hauppauge, NY, 2013; pp 403−418. DOI: 10.1016/B978-0-444-53175-9.00016-7.

(71) Hong, J.; Park, M. K.; Lee, E. J.; Lee, D.; Hwang, D. S.; Ryu, S. Origin of New Broad Raman D and G Peaks in Annealed Graphene. *Sci. Rep.* **2013**, *3*, No. 2700.

(72) Merlen, A.; Buijnsters, J. G.; Pardanaud, C. A Guide to and Review of the Use of Multiwavelength Raman Spectroscopy for Characterizing Defective Aromatic Carbon Solids: From Graphene to Amorphous Carbons. *Coatings* **2017**, *7*, 153−208.

(73) Wu, J. B.; Lin, M. L.; Cong, X.; Liu, H. N.; Tan, P. H. Raman Spectroscopy of Graphene-Based Materials and Its Applications in Related Devices. *Chem. Soc. Rev.* **2018**, *47*, 1822−1873.

(74) Sadezky, A.; Muckenhuber, H.; Grothe, H.; Niessner, R.; Pöschl, U. Raman Microspectroscopy of Soot and Related Carbonaceous Materials: Spectral Analysis and Structural Information. *Carbon* **2005**, *43*, 1731−1742.

(75) Dippel, B.; Jander, H.; Heintzenberg, J. NIR FT Raman Spectroscopic Study of Flame Soot. *Phys. Chem. Chem. Phys.* **1999**, *1*, 4707−4712.

(76) Wu, J.; Wang, P.; Wang, F.; Fang, Y. Investigation of the Microstructures of Graphene Quantum Dots (GQDs) by Surface-Enhanced Raman Spectroscopy. *Nanomaterials* **2018**, *8*, 864.

(77) Colomban, P.; Slodczyk, A. Raman Intensity: An Important Tool to Study the Structure and Phase Transitions of Amorphous/Crystalline Materials. *Opt. Mater.* **2009**, *31*, 1759−1763.

(78) Vyazovkin, S.; Koga, N.; Schick, C. *Handbook of Thermal Analysis and Calorimetry - Recent Advances, Techniques and Applications*, 2nd ed.; Elsevier, 2018; Vol. 6 DOI: 10.1016/B978-0-444-64062-8.00006-1.

(79) Tomić, N. Z. Chapter 17 - Thermal Studies of Compatibilized Polymer Blends. In *Compatibilization of Polymer Blends*; Ajitha, A. R.; Thomas, S., Eds.; Elsevier, 2020; pp 489−510 DOI: 10.1016/B978-0-12-816006-0.00017-7.

(80) Moldoveanu, S. C. Pyrolysis of Amines and Imines. In *Techniques and Instrumentation in Analytical Chemistry*; Elsevier, 2010; Vol. *28*, pp 349−364 DOI: 10.1016/S0167-9244(09)02813-3.

(81) Goodrum, J. W.; Siesel, E. M. Thermogravimetric Analysis for Boiling Points and Vapour Pressure. *J. Therm. Anal.* **1996**, *46*, 1251−1258.

(82) Tarasova, N. P.; Zanin, A. A.; Krivoborodov, E. G.; Mezhuev, Y. O. Elemental Sulphur in the Synthesis of Sulphur-Containing Polymers: Reaction Mechanisms and Green Prospects. *RSC Adv.* **2021**, *11*, 9008−9020.

(83) Zhang, Y.; Pavlopoulos, N. G.; Kleine, T. S.; Karayilan, M.; Glass, R. S.; Char, K.; Pyun, J. Nucleophilic Activation of Elemental Sulfur for Inverse Vulcanization and Dynamic Covalent Polymerizations. *J. Polym. Sci.* **2019**, *57*, 7−12.

(84) Miyazaki, T.; Nishino, K.; Yoshimoto, S.; Ogiwara, Y.; Sakai, N. Indium-Catalyzed Reductive Sulfidation of Aromatic Carboxylic Acids and Aldehydes with Elemental Sulfur to Prepare Symmetrical Benzyl Sulfides. *Eur. J. Org. Chem.* **2015**, *2015*, 1991−1994.

(85) Standard Guide for Raman Shift Standards for Spectrometer Calibration; Standard E1840-96; ASTM International, 2014. https://www.astm.org/e1840-96r14.html ( accessed 2022-07-06).

(86) Hagen, M.; Schiffels, P.; Hammer, M.; Dörfler, S.; Tübke, J.; Hoffmann, M. J.; Althues, H.; Kaskel, S. In-Situ Raman Investigation of Polysulfide Formation in Li-S Cells. *J. Electrochem. Soc.* **2013**, *160*, A1205−A1214.

(87) Hannauer, J.; Scheers, J.; Fullenwarth, J.; Fraisse, B.; Stievano, L.; Johansson, P. The Quest for Polysulfides in Lithium-Sulfur Battery Electrolytes: An Operando Confocal Raman Spectroscopy Study. *ChemPhysChem* **2015**, *16*, 2755−2759.

(88) McPhail, M. R.; Weiss, E. A. Role of Organosulfur Compounds in the Growth and Final Surface Chemistry of PbS Quantum Dots. *Chem. Mater.* **2014**, *26*, 3377−3384.

(89) Sudesh; Kumar, N.; Das, S.; Bernhard, C.; Varma, G. D. Effect of Graphene Oxide Doping on Superconducting Properties of Bulk MgB₂. *Supercond. Sci. Technol.* **2013**, *26*, No. 095008.

(90) Sodhi, R. K.; Paul, S. An Overview of Metal Acetylacetonates: Developing Areas/Routes to New Materials and Applications in Organic Syntheses. *Catal. Surv. Asia* **2018**, *22*, 31−62.

(91) Wu, X.; Smith, J. A.; Petcher, S.; Zhang, B.; Parker, D. J.; Griffin, J. M.; Hasell, T. Catalytic Inverse Vulcanization. *Nat. Commun.* **2019**, *10*, No. 647.

(92) Dodd, L. J.; Omar, Ö.; Wu, X.; Hasell, T. Investigating the Role and Scope of Catalysts in Inverse Vulcanization. *ACS Catal.* **2021**, *11*, 4441−4455.

(93) Dziemidkiewicz, A.; Maciejewska, M. Manganese and Nickel Acetylacetonates as Curatives for Chloroprene Rubber Based on Heck's Reaction. *Materials* **2021**, *14*, 807.

(94) Goetjen, T. A.; Liu, J.; Wu, Y.; Sui, J.; Zhang, X.; Hupp, J. T.; Farha, O. K. Metal-Organic Framework (MOF) Materials as Polymerization Catalysts: A Review and Recent Advances. *ChemComm.* **2020**, *56*, 10409−10418.

(95) Cheng, F.; Zhang, X.; Mu, K.; Ma, X.; Jiao, M.; Wang, Z.; Limpachanangkul, P.; Chalermsinsuwan, B.; Gao, Y.; Li, Y.; Chen, Z.; Liu, L. Recent Progress of Sn-based Derivative Catalysts for Electrochemical Reduction of CO₂. *Energy Technol.* **2021**, *9*, No. 2000799.

(96) Gawande, M. B.; Goswami, A.; Felpin, F.-X.; Asefa, T.; Huang, X.; Silva, R.; Zou, X.; Zboril, R.; Varma, R. S. Cu and Cu-Based Nanoparticles: Synthesis and Applications in Catalysis. *Chem. Rev.* **2016**, *116*, 3722−3811.

(97) Ain, N. ul.; Zia-ur-Rehman; Aamir, A.; Khan, Y.; Rehman, M.; Lin, D.-J. Catalytic and Photocatalytic Efficacy of Hexagonal CuS Nanoplates Derived from Copper(II) Dithiocarbamate. *Mater. Chem. Phys.* **2020**, *242*, No. 122408.

(98) Hunge, Y. M.; Yadav, A. A.; Liu, S.; Mathe, V. L. Sonochemical Synthesis of CZTS Photocatalyst for Photocatalytic Degradation of Phthalic Acid. *Ultrason. Sonochem.* **2019**, *56*, 284−289.

(99) Jayaraman, V. K.; Hernández-Gordillo, A.; Bizarro, M. Importance of Precursor Type in Fabricating ZnO Thin Films for Photocatalytic Applications. *Mater. Sci. Semicond. Process* **2018**, *75*, 36−42.

(100) Cova, C. M.; Zuliani, A.; Muñoz-Batista, M. J.; Luque, R. A Sustainable Approach for the Synthesis of Catalytically Active Peroxidase-Mimic ZnS Catalysts. *ACS Sustainable Chem. Eng* **2019**, *7*, 1300−1307.

(101) Maarof, S.; Ali, A. A.; Hashim, A. M. Synthesis of Large-Area Single-Layer Graphene Using Refined Cooking Palm Oil on Copper Substrate by Spray Injector-Assisted CVD. *Nanoscale. Res. Lett.* **2019**, *14*, No. 143.

(102) Bajpai, P. K.; Yadav, S.; Tiwari, A.; Virk, H. S. Recent Advances in the Synthesis and Characterization of Chalcogenide Nanoparticles. *Solid State Phenom.* **2014**, *222*, 187−233.

(103) Malik, M. A.; Afzaal, M.; O'Brien, P. Precursor Chemistry for Main Group Elements in Semiconducting Materials. *Chem. Rev.* **2010**, *110*, 4417−4446.

(104) Khan, M. D.; Malik, M. A.; Revaprasadu, N. Progress in Selenium Based Metal-Organic Precursors for Main Group and Transition Metal Selenide Thin Films and Nanomaterials. *Coord. Chem. Rev.* **2019**, *388*, 24−47.